

國立臺灣大學理學院海洋研究所

碩士論文

Graduate Institute of Oceanography

College of Science

National Taiwan University

Master Thesis

海流流速估算內孤立波海底壓力變化

**Seafloor pressure variation of internal solitary wave
estimated from current velocity**



楊馨維

Ching-Wei Yang

指導教授：唐存勇 博士、楊穎堅 博士

Advisors : Tswen-Yung Tang, Ph.D., Ying-Jang Yang, Ph.D.

中華民國 100 年 7 月

July, 2011

中文摘要

北南海內孤立波盛行，世界觀測紀錄上最大等密面垂直位移之內孤立波即量測於此。2007 年，兩組錨錠測站施放於北南海大陸棚斜坡上用以量測內孤立波流速場以及海底壓力之變化。流速觀測結果顯示，內孤立波以第一斜壓模下沉型為主。海底壓力量測結果顯示潮汐壓力振幅大約為 0.5 至 2 分巴，內孤立波壓力振幅大約為 0.05 至 0.35 分巴。本研究選用 38 個壓力振幅大於 0.05 分巴的內孤立波研究並估算其壓力變化。使用經背景場校正後的垂直接流速資料，並對其進行時間積分以估算內孤立波振幅。內孤立波的波速則是利用波傳方向之二維連續方程計算。內孤立波的波傳方向是以上層海流方向估算之。計算所得之振幅、波速、波向並可用於音響式都卜勒流剖儀(Acoustic Doppler Current Profiler, ADCP)束散效應(beam-spreading effect, Scotti *et al.*, 2005)的校正。校正後之 ADCP 流速資料配合垂直動量方程式與白努力方程式，可計算內孤立波之非靜水壓以及海床壓力變化。結果顯示，計算所得之海床壓力變化與量測的結果近乎一致，而內孤立波之非靜水壓變化與量測的海床壓力變化成正比，內孤立波之海床壓力變化亦與內孤立波振幅成正比，而此兩者之間的線性迴歸經驗關係式可應用於以海底壓力資料估算內孤立波振幅大小。

關鍵字：南海、內孤立波、垂直振幅、海床壓力、非靜水壓。

Abstract

The internal solitary waves (ISWs) are active and have large amplitude in the northern South China Sea. Two mooring sets, each set contains an Acoustic Doppler Current Profiler (ADCP) and a bottom-mounted pressure gauge, were deployed on the continental slope of the northern South China Sea. The mode-1 depression ISWs were clearly seen in the observed current velocity. The ISWs could induce 0.05-0.35 dbar of pressure fluctuation while the tides caused around 0.5-2 dbar of pressure fluctuations. 38 ISWs, caused pressure fluctuations larger than 0.05 dbar, were chosen to study the wave properties. The near bottom pressure disturbances which estimated from current velocity data are compared with the observation. The non-hydrostatic pressure disturbances are also calculated and discussed.

The ISW vertical displacement was estimated from the time integration of vertical velocity with the correction of heave motion of background flow. The ISW propagation speed was estimated from the continuity equation. The wave propagation direction was the same as the direction of upper ocean current caused by ISW. These wave properties were used to estimate the current velocities of ISW by calibrating the beam-spreading effect of ADCP measurement. The non-hydrostatic and near bottom pressure disturbances of ISW were estimated from the calibrated current velocities by using the vertical momentum and Bernoulli equations,

respectively.

The result indicates that the estimated ISW bottom pressure variation could represent the observed pressure variation at bottom. The estimated ISW non-hydrostatic pressure variation and the ISW maximum vertical displacement were proportional to the bottom pressure perturbation. A conclusion is obtained that both the maximum vertical displacement and non-hydrostatic pressure variation caused by the mode-1 depression ISW in the northern SCS could be estimated from the bottom pressure gauge.



Key words: South China Sea, internal solitary wave, vertical displacement, bottom pressure disturbance, non-hydrostatic pressure.

Contents

Contents.....	i
Figure Caption.....	ii
Table List.....	iv
Symbol Table.....	v
Acronym Table.....	vii
I. Introduction.....	1
II. Observations.....	5
<2-1 Field works>.....	5
<2-2 Data>.....	9
III. Data processes and methods.....	18
< 3-1 Near bottom pressure signals of ISW>.....	18
< 3-2 Computation of ISW properties from ADCP data >.....	21
< 3-3 Decomposed near bottom pressure signals of ISW >.....	23
IV. Results.....	27
< 4-1 Properties of ISWs >	27
< 4-2 Non-hydrostatic pressure >.....	44
< 4-3 Total near bottom pressure >.....	31
V. Discussion and Summary.....	39
< 5-1 ISW pressure and vertical displacement >.....	39
< 5-2 Summary >.....	40
Appendix.....	42
References.....	46

Figure Caption

Fig.2-1	(a) Bathymetry in South China Sea and (b) Diagram of mooring scheme.....	6
Fig.2-2	Time series at station LR1 including the current velocity U , V and W at 104-m and 312-m. Bottom panel is the near bottom pressure fluctuations.....	11
Fig.2-3	Time series at station LR4 including the current velocity U , V and W at 56-m and 240-m, Bottom panel is the near bottom pressure fluctuations.....	13
Fig.2-4	Bottom pressure fluctuation time series from LR1. (a) raw data. (b) low-pass filter with cutoff period at 1 hour. (c) high-pass filter with cutoff period at 1 hour.....	15
Fig.2-5	Bottom pressure fluctuation time series from LR4. (a) raw data. (b) low-pass filter with cutoff period at 1 hour. (c) high-pass filter with cutoff period at 1 hour.....	15
Fig.2-6	The raw data of horizontal and vertical current velocity and the near bottom pressure signature of an internal solitary wave of depression passing station LR1 on 17 Apr 2007.....	17
Fig.3-1	The results of extracting pressure perturbation associated with ISW between different methods.....	20
Fig.4-1	Wave properties before iterative algorithm.....	28
Fig.4-2	Wave properties after iterative algorithm.....	28

Fig.4-3 The upper two panels shows the time-varying horizontal velocity, u' , and vertical velocity, w , of a solitary internal with the correction of beam separate effect. The lower three panels shows the component terms of P_{nh} : $\partial w/\partial t$, $u'\partial w/\partial x$, $w\partial w/\partial z$, respective. The bottom panel is the total vertical acceleration, Dw/Dt ,32

Fig.4-4 The total near bottom pressure disturbance estimated using Bernoulli function ($P_{Estimate}$, blue line) and the near bottom non-hydrostatic pressure disturbance (P_{nh} , green line)34

Fig.4-5 The comparison of the normalized near bottom pressure disturbance between estimated and measured pressure at (a) station LR1 and (b) station LR4.....36

Fig.4-6 Comparison of the maximum amplitude between measured near bottom pressure and the estimated (blue dots); and the maximum amplitude between measured near bottom pressure and non-hydrostatic pressure (red dots) at (a) station LR1 and (b) station LR4.38

Fig.5-1 Comparison between amplitude of $P_{Measure}$ and η at LR1 (blue dots) and LR4 (red dots), respectively.....39

Table List

Tab. 2-1	Summary of moorings information.....	8
Tab. 4-1	The ISWs at station LR1.....	29
Tab. 4-2	The ISWs at station LR4.....	30



Symbol Table

B	Bernoulli constant
C	wave propagation speed
$P_{Estimate}$	near bottom pressure perturbation caused by internal solitary wave estimated from ADCP data
$P_{Measure}$	near bottom pressure perturbation caused by internal solitary wave measured from pressure gauge
P_h	hydrostatic pressure perturbation caused by internal solitary wave
P_{hn}	external hydrostatic pressure perturbation caused by internal solitary wave
P_{hp}	internal hydrostatic pressure perturbation caused by internal solitary wave
P_{nh}	non-hydrostatic pressure perturbation caused by internal solitary wave
U	zonal velocity
U_b	zonal background velocity
U_b'	background velocity along wave direction
V	meridional velocity
V_b	meridional background velocity
V_b'	background velocity across wave direction
W	vertical velocity
W_b	vertical background velocity
b_1	along-beam velocity of ADCP beam one
b_2	along-beam velocity of ADCP beam two
b_3	along-beam velocity of ADCP beam three
b_4	along-beam velocity of ADCP beam four
d	vertical distance from the transducer head
hd	ADCP heading
t	time parameter
u	zonal velocity perturbation caused by internal solitary wave
u'	velocity perturbation along wave direction caused by internal solitary wave
v	meridional velocity perturbation caused by internal solitary wave velocity

v'	velocity perturbation across wave direction caused by internal solitary wave
w	vertical velocity perturbation caused by internal solitary wave
x	eastward
x'	along wave propagation direction
y	northward
y'	across wave propagation direction
z	upward
z_p	0.5 m off the bottom
z_p'	30 m off the bottom
ϕ	angle of the transducer head from vertical
η	vertical displacement (isopycnal displacement)
θ	wave propagation direction (respect to the east-west axis)
θ_0	wave propagation direction (respect to the b1-b2 axis)
ρ_0	ambient density
$\rho_b(z)$	vertical density profile
$\rho_w(x, z, t)$	density perturbation associated with the internal solitary wave
ψ_0	bottom streamline
∂	partial differential

Acronym Table

ADCP	Acoustic Doppler Current Profiler
EMD	Empirical Mode Decomposition
IMF	Intrinsic Mode Function
ISW	Internal Solitary Wave
SCS	South China Sea
PIES	Pressure sensor equipped Inverted Echo-Sounders



I. Introduction

Internal Solitary Waves (ISWs) are ubiquitous in the world ocean (Apel *et al.*, 2007). It could be generated when the currents flow over an irregular topography in stratified water (Famer and Armi, 1999). In the open ocean, ISWs could propagate over hundreds of kilometers without changing their shapes. Most of them are first baroclinic mode (mode-1) depression waves which cause downwellings followed by upwellings. The mode-1 ISW has the horizontal velocities out of phase between the upper and lower oceans, respectively. Theoretically, mode-1 ISW propagates with the direction of horizontal velocity in the upper ocean caused by itself. As the ISW propagate into a shallow water region, it could have phase speed decrease, dissipation increase, transformation, refraction, mixing increase, and breaking, etc. (Haury *et al.*, 1979; Alford *et al.*, 2010). A depression wave sometimes could even transform to an elevation wave whose upwelling lead downwelling (Liu *et al.*, 1985). The ISW also could have many influences on the oceanic environment. For example, it could have notable impacts on the submarine navigation safety, underwater acoustic propagation, offshore structure, and vertical mixing, etc.. Because its importance, it has been drawn a lot of attention, especially in the South China Sea (SCS) on last decade.

In the northern SCS, large-amplitude nonlinear ISWs were often observed (Hsu *et al.*, 2000; Yang *et al.*, 2004; Chang *et al.*, 2006; Alford *et al.*, 2010). Most of the ISWs in the SCS are generated by the internal tide (Duda *et al.*, 2004; Ramp *et al.*, 2004; Alford *et al.*, 2010). Internal tides were generated by the barotropic tides flow over the ridge in the Luzon Strait. (Niwa and Hibiya, 2004; Jan *et al.*, 2007). Observations also found that the largest amplitude of ISWs in the world was in the SCS (Ramp *et al.*, 2004), they identified that the trans-basin ISW had amplitudes ranging from 29 m to greater than 140 m, and the observed vertical velocity as large at 60 cm/s. Yang *et al.* (2004) founded that the largest observed horizontal current speed caused by the ISW was 240 cm/s at the upper layer and 150 cm/s at the lower layer, and the largest temperature fluctuation was 11°C. The crest of the ISW could reach 200 km (Liu *et al.*, 1998).

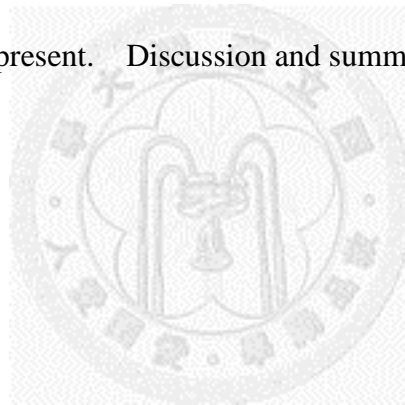
Beside the current and hydrographic data, the bottom pressure signal of ISW could also study. For example, Li *et al.* (2009) used the pressure sensor equipped inverted echo-sounders (PIES) to observe ISW in the basin of SCS. Their measurements show a pressure decrease of about 0.04 dbar associated with an ISW of amplitude around 100 m which estimated from the KdV model. Moum and Smyth (2006) applied the observations of the bottom pressure signals, ADCP velocity

measurements and repeated hydrographic vertical profiles to study the seafloor pressure disturbance of elevation internal waves over the continental shelf off Oregon. The peak of the estimated seafloor pressure of an elevation ISW was $O(100)$ N/m², equivalent to about 0.01 dbar. Similarly, Moum and Nash (2008) used the same methods to investigate depression internal waves over the New Jersey shelf. The peak of the estimated seafloor pressure of a depression ISW was 765 Pa, equivalent to about 0.0765 dbar. These studies concluded that the positive and negative seafloor pressure anomalies are caused by the elevation and depression ISW, respectively.

The repeated hydrographic profile measurement has difficulty to be performed in the SCS due to the fishery activities. A method only used moored ADCP and bottom mounted pressure gauge is developed in this thesis to perform similar study of Moum and Smyth (2006) and Moum and Nash (2008) but in the SCS. The method adapts the iterative algorithm developed by Chang *et al.* (2011) to properly estimate the propagation direction and phase speed of ISW. Therefore, the measurement of hydrographic profile, used to estimate the phase speed, is not required. However, the method has limitation, without the hydrographic profiles only non-hydrographic pressure perturbation is estimated. It is interesting to point out that the near bottom pressure variation caused by the ISW could be re-constructed with acceptable error

using only ADCP current velocity.

The organization of this thesis as follows. The experiment and instruments are described in Section 2. In Section 3, data processing and methodology used are presented, including the extraction of pressure perturbation and velocity disturbance associated with ISW, and the decomposition of bottom pressure perturbations due to an ISW. In Section 4, the computation of the decomposed bottom pressure components and the comparison between estimated and observed near bottom pressure perturbations are present. Discussion and summary are show in Section 5.



2. Observations

<2-1 Field works>

Two mooring sets were deployed on the continental slope in the northern SCS in 2007. The location and diagram of moorings are shown in Fig. 2-1. The upper panel of Fig. 2-1 shows the bathymetry in northern SCS, the asterisks represent the location of two mooring stations, named LR1 and LR4. The local depths were 605-m and 340-m at LR1 and LR4, respectively. The mooring diagram is shown in the lower panel, which is similar for both LR1 and LR4. Each mooring set contains a moored ADCP and a bottom-mounted pressure gauge. The upward-looking, 75 kHz ADCP with 20° transducer was mounted inside a 45” syntactic foam buoy at a depth of about 10 m above the bottom to measure the near full-depth current velocity. Next to the ADCP mooring, a bottom-mounted pressure gauge was deployed separately to measure the near bottom pressure variations.

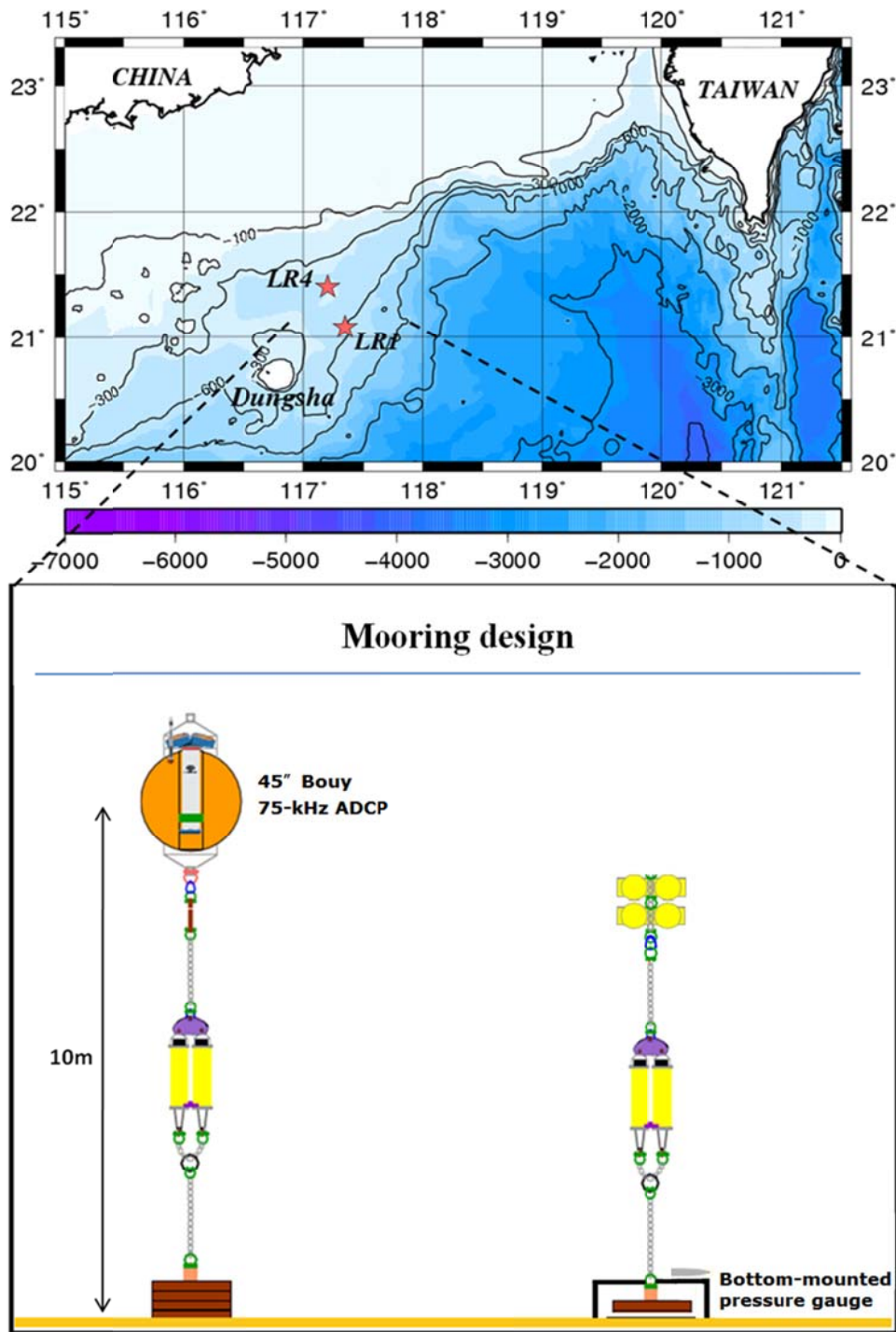


Fig. 2-1: (a) Bathymetry in South China Sea, the asterisks represent the location of mooring sets. (b) The diagrams of subsurface ADCP mooring and bottom-mounted pressure gauge.

The durations of the deployments of ADCP moorings and pressure gauges were inconsistent at both LR1 and LR4. The overlap period was April 13 to May 7 at station LR1 and April 13 to June 11 at station LR4 in 2007, respectively. The ADCP's sampling rates were 90 s and 30 s on LR1 and LR4, respectively. The blanking distance of ADCP velocity measurements from the transducer head was 8 m at both stations. The current velocity was obtained from 56 m to 568 m with 16 m bin length at LR1 and from 32 m to 312 m with 8 m bin length at LR4, respectively. The velocity near the sea surface was excluded because of the contamination of surface reflection. The mooring platform was generally stable. The vertical excursions were within 4 m at LR1 and 3 m at LR4, respectively. The tilt sensor data show that the maximum tilt angle was around 15° and 10° at LR1 and LR4, respectively, but most of the tilt angle were less than 6° at both LR1 and LR4. The bottom-mounted pressure gauge collected discrete samples at 60 s and 90 s intervals on LR1 and LR4, respectively. Tab. 2-1 shows the summary of moorings information.

Tab. 2-1

Summary of moorings information

Station	Bottom depth (m)	Latitude	Longitude	Instr. depth (m)	Start	Stop	Sampling rate (min)	ADCP bin length (m)	Pressure gauge resolution (dbar)
LR1	605	21.09	117.35		4/13/2007 00:33:00	5/7/2007 02:12:00			
ADCP 75-kHz				594.2±0.9			1.5	16	
SBE-39(1000-m)				612			1		0.02
LR4	340	21.40	117.20		4/13/2007 10:30:00	6/11/2007 21:51:00			
ADCP 75-kHz				329.3±0.7			0.5	8	
SBE-39(600-m)				344			1.5		0.012

<2-2 Data>

The raw current velocity recorded by ADCP was in earth coordinates. Fig. 2-2 shows the current velocity and near bottom pressure at LR1. From top to the bottom, there have 7 panels. They are the zonal velocity (U), meridional velocity (V) and vertical velocity (W) at 104 m and 312 m and the near bottom pressure sequentially. The mean of U at 104 m and 312 m were around -0.05 m/s and -0.01 m/s, respectively. And the mean of V at 104 m and 312 m were around -0.05 m/s and -0.04 m/s, respectively. The subtidal current was generally weak. The spectra analysis (not shown) indicates the current variations dominated by the diurnal and semidiurnal tides. The fortnightly variation was clearly seen. The diurnal tide dominated during the spring tide while both the diurnal and semidiurnal were seen during the neap tide. The vertical structure of tidal currents were not uniform, it might associated with the baroclinic motions. The W current velocity fluctuation was generally weak, around 0.10 m/s at the spring tide and around 0.03 m/s at the neap tide.

For the super-tidal variation, the most remarkable feature was a number of large spike-like fluctuations, especially in U and W . Such fluctuation indeed was presented in either V or P but dimly. The spike-like fluctuations of U at 104 m and 312 m were generally westward and eastward, respectively. Further examined the U

and W over the whole water column for the spike-like fluctuation and found that U was out of phase between upper and lower water with a nodal point around 220 m, and the W current velocity has a downwelling followed by a upwelling with relatively large velocity at middle depths. These results indicate that the spike-like fluctuations could be caused by the mode-1 depression ISWs. The spike-like fluctuations of V were small that could relate with the mode-1 ISWs propagated primarily westward (Ramp *et al.*, 2004).

The pressure data displayed the diurnal and semidiurnal tidal variations clearly. Large fortnightly variations were also seen. The barotropic tides at LR1 caused around 1.2 dbar and 0.5 dbar variations at the spring and neap tides, respectively. The pressure fluctuations caused by ISWs were seen, but hardly to give a quantitative description. Further analysis is shown later.

Similar to Fig. 2-2, Fig. 2-3 shows the current velocity at 56 m and 240 m and the near bottom pressure fluctuations at LR4. It is worthy to point out that the length of time series at LR4 was two months, which is much longer than it at LR1.

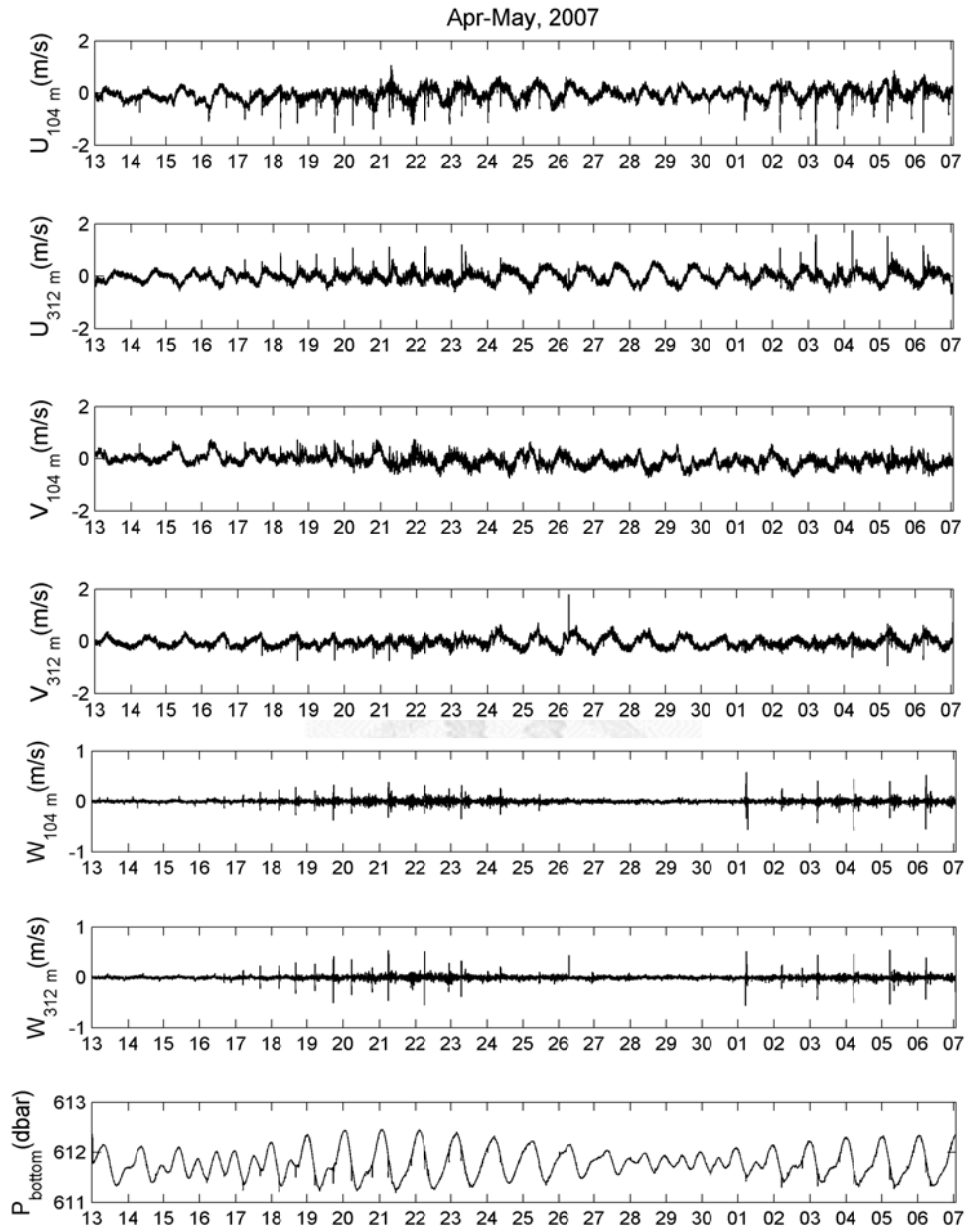


Fig.2-2: Time series at LR1 including the U , V , and W current velocities at 104-m and 312-m, and the near bottom pressure fluctuations.

Comparable to the LR1, the mean current of U and V were small, the subtidal current was generally weak and diurnal tidal current dominated during the spring tide while the semidiurnal tide became more pronounced during the neap tide. The baroclinic tidal current again was seen. The barotropic tide could induce 0.8 and 0.3 dbar pressure variation in the spring and neap tide, respectively.

The spike-like fluctuations, which could be caused by the mode-1 depression ISWs, were also seen at LR4. Because the ISW could evolve into a series of wave trains and its amplitude could reduce when it propagated into the shallow water, it became difficult to identify. However, the characteristics of mode-1 depression ISW were seen. For example, the horizontal current velocity was out of phase, the vertical current velocity has a downwelling followed by an upwelling etc. In order to perform the present study, a criterion of pressure variation is given to choose the most notable waves. The criterion is stated in the next paragraph. The bottom-mounted pressure gauge has a slight slide on May 06 12:18 while a large ISW passed by. However, the excursion was removed by shifting the pressure data, and the ISW event was excluded from the following analysis.

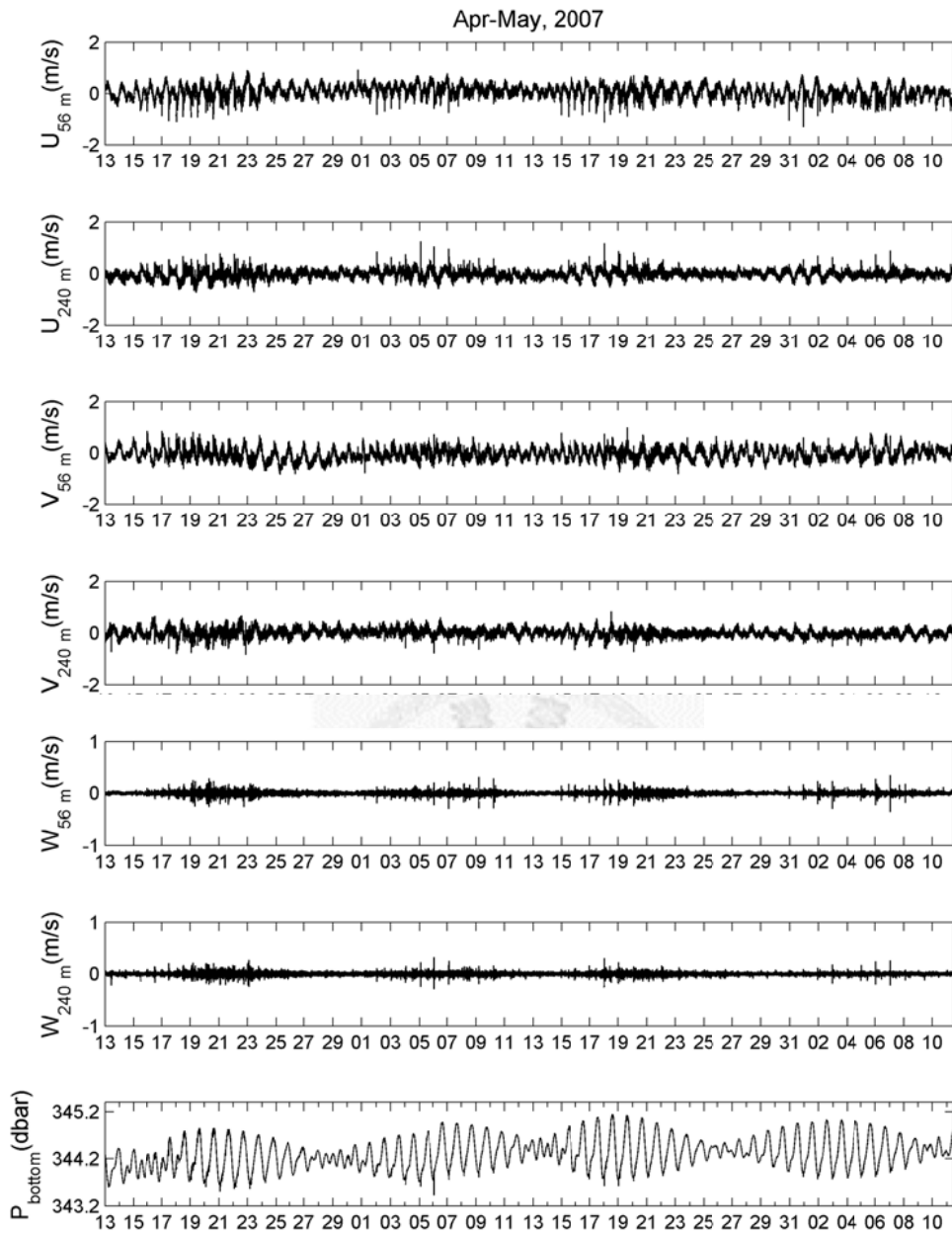


Fig.2-3: Time series at LR4 including the current velocity U , V and W at 56 m and 240 m, and the near bottom pressure fluctuations.

The one hour high-pass filtered pressure time series was calculated. The obtained time series was used to quickly choose the most notable ISW. Figs. 2-4 and 2-5 show the results at LR1 and LR4, respectively. The top panel in each figure shows the one hour high-passed filtered pressure variation. The ISW events are now more distinguishable. It induced the pressure fluctuation around 0.03-0.25 dbar at LR1, and around 0.02-0.20 dbar at LR4, respectively. Only the fluctuation had amplitude large than 0.05 dbar is considered in this study. Panel (b) in each figure shows the selected large fluctuation marked by black sticks along with the raw pressure variation. The large ISW, indicated by the black stick, occurred generally in the spring tide duration. This result is consistent with the former studies (Ramp et al., 2004; Yang et al., 2004). Most of selected ISWs are the leading wave of wave trains.

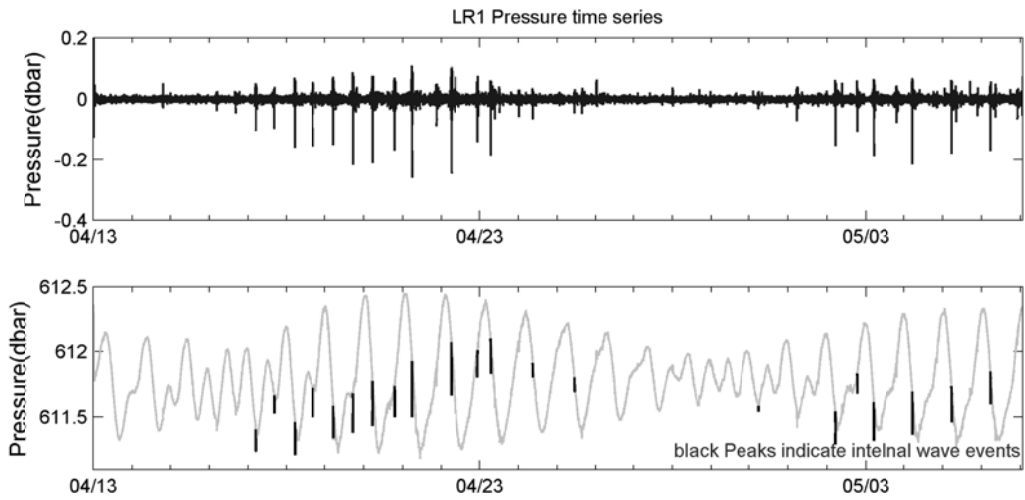


Fig. 2-4 Bottom pressure fluctuation time series from LR1. (a) High-pass filter with cutoff period at 1 hour. (b) Raw data. The black sticks indicated the ISW events.

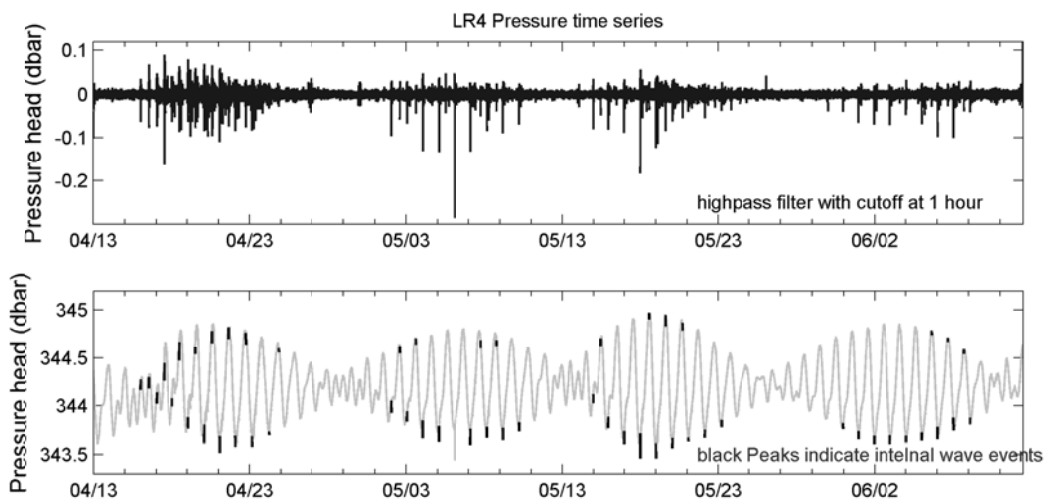


Fig. 2-5 Same as Fig. 2-4, except at LR4.

The current velocity distribution at LR1 on 17 Apr 2007 16:47 when the large pressure fluctuation was seen is shown in Fig. 2-6. From top to the bottom panels, are the current velocity U , V , W and the near bottom pressure variation. This wave was similar in form to waves observed at northeast of Dong-Sha Island in previous studies (Duda *et al.*, 2004; Ramp *et al.*, 2004 & 2010; Yang *et al.*, 2004). It caused a negative surge in U (westward acceleration) at the upper layer; reversed (eastward acceleration) at the lower layer and has a downwelling followed by an upwelling at W . The maximum peak of the bottom pressure signal was above the wave core and has positive sign with the vertical fluid accelerations (isopycnal displacement). These concluded that the wave was a mode-1 depression ISW. The wave was chosen for the example to exhibit on the following articles.

The raw data of current velocities and near bottom pressure variation contained the signals of ISWs, tides and background flows. The processes of separating ISW from raw data are introduced at section 3.

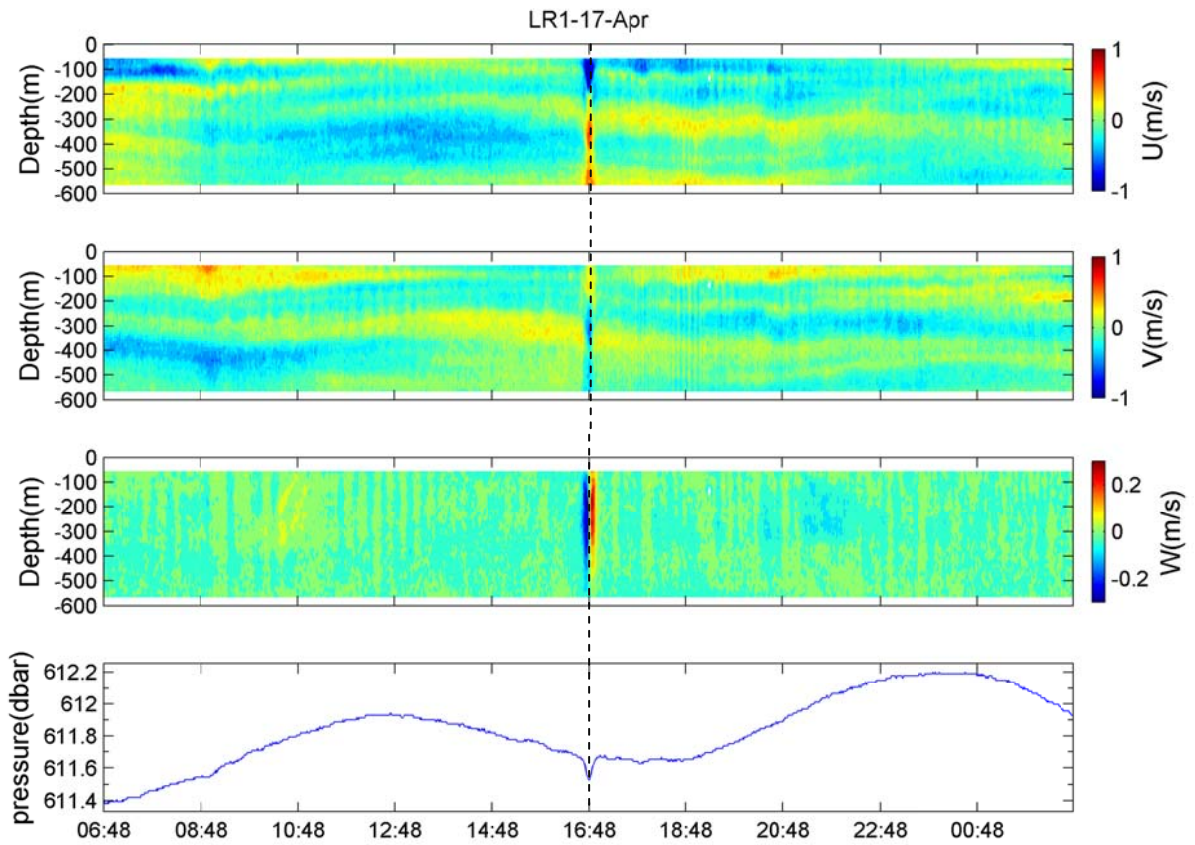


Fig. 2-6 The raw data of U , V , and W current velocity and the near bottom pressure variation of an mode-1 depression ISW passing LR1 on 17 Apr 2007.

3. Data processes and methods

< 3-1 Near bottom pressure signals of ISW >

There were four methods, high-pass filtration, harmonic analysis, Empirical Mode Decomposition (EMD, Huang *et al.*, 1998), and linear extracting method, were applied to extract the relatively high-frequency ISW pressure signal (typical amplitude 0.05-0.35 dbar; time scale 15-25 min) from the observed near bottom pressure variation (0.5-1.5 dbar). The differences of results among these methods were discussed.

The cut off period was 1 hour for the high-pass filter. Since the tides are the dominate influence on the near bottom pressure disturbance, the harmonic analysis was applied to remove tidal components from raw data. Harmonic analysis modeled tidal signal as the sum of a finite set of sinusoids at specific frequencies related to astronomical parameters. The T-Tide (Pawlowicz *et al.*, 2002) program was used to perform harmonic analysis. The EMD method was developed for analyzing nonlinear and non-stationary data with which any complicated data set can be decomposed into a finite and often small number of Intrinsic Mode Functions (IMFs). This decomposition is based on the local characteristic time scale of the data. The linear extracting method is an artificial process which extracting ISW signal from

observation by constructs a new pressure time series excluding low frequency components and linearly interpolating the missing pressure segment. All the identified ISW pressure events from these filtering processes have been reconfirmed with the velocity measurement.

The comparison of results from four methods for the example ISW is shown in Fig. 3-1. Fig. 3-1 (a) shows the observed pressure including the example ISW event (black curve) and the filtered pressure signals from four methods: high-pass filter (blue curve), harmonic analysis (green curve), linear extracting method (pink curve), and EMD method (gray curve). Fig. 3-1 (b) shows the extracted ISW pressure signal, the arrow lines indicate the filter effects, which could reducing the ISW signal around the center of the wave and adding artificial perturbations around the front and rear ends of the wave.

Considering these artificial effects might affect the comparison between observed and estimated pressure, we ultimately chose the linear extracting method for ISW pressure data process.

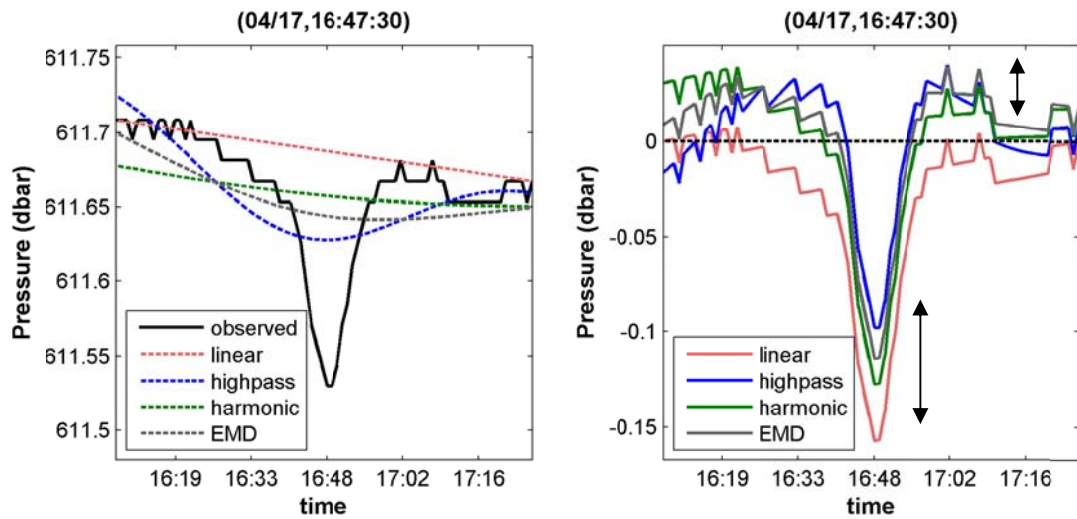


Fig. 3-1 Panel (a) shows the observed pressure including one ISW event (black curve) and the filtered pressure signals from four methods: high-pass filter (blue curve), harmonic analysis (green curve) and linear extracting method (pink curve), and EMD method (gray curve). Panel (b) shows the extracted ISW pressure signals. The arrow lines indicate the filter effects.

< 3-2 Computation of ISW properties from ADCP data >

Similar with the pressure data, extracting the current velocity associate with ISW from ADCP raw data is difficult. Besides, the current velocities of ISW measured by ADCP could have beam-spreading effect (Scotti *et al.*, 2005). While measure current velocity using ADCP, beam-spreading effect increases to several hundred meters at great range, which introduces errors in velocity estimates when ISW widths are comparable or smaller. The corrected current velocities and wave properties were need to further estimate the bottom pressure disturbance caused by ISW (section 3-3).

Followed Chang *et al.*, 2011, an iterative method was applied for correcting the ISW signal and estimating the wave properties from moored ADCP measurements.

The wave properties included the vertical displacement (η), the wave propagation direction (θ), and the wave propagation speed (C). Both earth (x, y, z) and wave-oriented (x', y', z) coordinates are used. The apostrophe (') denotes the wave-oriented coordinates. The x, y, z represent the eastward, northward and upward coordinates, respectively. The x' and y' represent the along and cross ISW propagation direction, respectively. Total velocities in earth coordinates are expressed as (U, V, W). The background velocities in earth and wave-oriented

coordinates are expressed as (U_b, V_b, W_b) and (U_b', V_b', W_b') , respectively. The current velocities caused by the ISW in earth and wave-oriented coordinates are expressed as (u, v, w) and (u', v', w) .

The iteration begins from the estimate of the vertical displacement

$$\eta = \int \frac{w}{1 - U_b'(z - \eta)/C} dt, \quad (3.1)$$

with the initial guess $\eta = \int w dt$, and t is the time parameter. The propagation direction θ can be estimated, after subtracting the modulated background flow, using

$$\theta = \tan^{-1} \frac{V - V_b(z - \eta)}{U - U_b(z - \eta)}. \quad (3.2)$$

After rotating the system to wave coordinate (x', y') using the estimate of θ . The wave speed C is obtained using the 2-D continuity equation

$$C = \frac{\partial u'}{\partial t} \Big/ \frac{\partial w}{\partial z} = \frac{\partial(u \cos \theta + v \sin \theta)}{\partial t} \Big/ \frac{\partial w}{\partial z}. \quad (3.3)$$

The estimated wave direction θ and wave speed C are used to perform phase-lagged beam-to-earth transformation for the beam-spreading effect correction

$$(u, v, w) = \left(\frac{n_1 - n_2}{2 \sin \phi}, \frac{n_3 - n_4}{2 \sin \phi}, \frac{n_1 + n_2 + n_3 + n_4}{4 \cos \phi} \right), \quad (3.4)$$

where

$$n_1 = b_1(t - s_x/2), \quad n_2 = b_2(t + s_x/2), \quad n_3 = b_3(t - s_y/2), \quad \text{and} \quad n_4 = b_4(t + s_y/2),$$

$$s_x = 2d \tan(\phi) \cos(\theta + hd)/C, \quad s_y = 2d \tan(\phi) \sin(\theta + hd)/C, \quad \text{here, } b_1, b_2, b_3,$$

and b_4 are along-beam velocity components of four ADCP beams, d is the vertical

distance from the transducer head, ϕ is the angle of the transducer head from vertical, hd is the ADCP heading. The schematic of the coordinate system for phase-lagged beam-to-earth transformation is shown in Appendix.

After remove the beam spreading effect, then go through all above and procedure repeatedly. It continues until the estimated η , θ and C approach the minimum variability (unvaried floor).

< 3-3 Decomposed near bottom pressure signals of ISW >

The pressure field of an ISW may be decomposed into a hydrostatic, P_h , and a nonhydrostatic, P_{nh} , parts from the vertical momentum equation as described subsequently. The hydrostatic part includes the external hydrostatic pressure, $P_{h\eta}$, from the surface elevation, and the internal hydrostatic pressure, P_{hp} , caused by isopycnal displacement, so that $P_h = P_{h\eta} + P_{hp}$. Therefore, the near bottom pressure signal of an ISW was decomposed into three components, P_{nh} , $P_{h\eta}$, and P_{hp} . The P_{hp} related to density profile ($\rho(x, z, t)$), it is defined as the sum of ambient density (ρ_0), vertical density profile ($\rho_b(z)$), and perturbation associated with the ISW ($\rho_w(x, z, t)$):

$$\rho(x, z, t) = \rho_0 + \rho_b(z) + \rho_w(x, z, t). \quad (3.5)$$

Follow Moun and Smyth (2006), we consider the near bottom pressure associated with a two-dimensional ISW steady passing the mooring site with propagation speed C . The vertical momentum equations for a non-rotating, inviscid, Boussinesq fluid may be described as

$$\frac{\partial P}{\partial z} = -\rho g - \rho_0 \frac{Dw}{Dt}. \quad (3.6)$$

where

$$\frac{D}{Dt} \equiv \frac{\partial}{\partial t} + u' \frac{\partial}{\partial x} + w' \frac{\partial}{\partial z}, \quad (3.7)$$

P is the ISW seafloor pressure disturbance, and g is the gravitational acceleration.

Consider a wave travelling without change of form and propagation speed, the partial time derivative may be written as

$$\frac{\partial}{\partial x} = -\frac{1}{C} \frac{\partial}{\partial t}. \quad (3.8)$$

Vertical integration of Eq. (3.6) from seafloor, $z = 0$, to a undisturbed water depth, $z =$

H , leads to

$$P = P_h + P_{nh}, \quad (3.9)$$

or

$$P = P_{h\eta} + P_{h\rho} + P_{nh}. \quad (3.10)$$

The $P_{h\eta}$ is the external hydrostatic pressure from the surface elevation

$$P_{h\eta} = \rho_0 g \eta_H, \quad (3.11)$$

where η_H is the surface elevation. The P_{hp} is the internal hydrostatic pressure caused by isopycnal displacement

$$P_{hp} = g \int_0^H \rho_w dz. \quad (3.12)$$

The P_{nh} is the non-hydrostatic pressure

$$P_{nh} = \rho_0 \int_0^H \frac{Dw}{Dt} dz. \quad (3.13)$$

The ISW seafloor pressure disturbance (P) can independently estimate through Bernoulli's principle. Bernoulli's principle relates the velocity and the pressure in a fluid, and may be derived from the momentum equation (see, for instance Kundu, 1990). The Bernoulli equation in an inviscid fluid described as

$$B = \frac{1}{2}(u^2 + v^2 + w^2) + gz + \frac{P}{\rho}. \quad (3.14)$$

B is the Bernoulli constant. With our assumption mentioned before (a 2-D ISW steady passing the mooring site with constant propagation speed C), the Bernoulli equation become

$$B = \frac{1}{2}[(u' - C)^2 + w^2] + gz + \frac{P}{\rho}. \quad (3.15)$$

The Bernoulli constant B must be constant along a streamline, and the zero-normal flow condition assures that the bottom boundary is a streamline (ψ_0):

$$B(\psi_0) = \frac{1}{2}\{[u'(\psi_0) - C]^2 + w^2\} + gz(\psi_0) + \frac{P(\psi_0)}{\rho} = B_0. \quad (3.16)$$

The vertical velocity and vertical displacement vanish because the assumed flat

streamline (bottom boundary) and the horizontal current and pressure perturbations vanish at the background. The pressure sensor is located z_p , 0.5 m off the bottom which should be a good approximation for the streamline. Therefore,

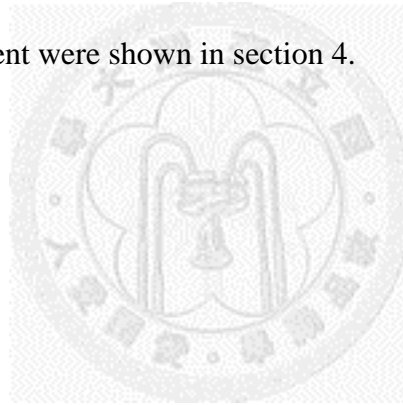
$$B(z_p) = \frac{1}{2} \{ [u'(z_p) - C]^2 \} + \frac{P(z_p)}{\rho} = \frac{1}{2} C^2, \quad (3.17)$$

According to the Bernoulli equation, the pressure perturbation at z_p is

$$P(z_p) = \frac{\rho}{2} \{ C^2 - [u'(z_p) - C]^2 \}. \quad (3.18)$$

The results of decomposed seafloor pressure disturbance estimated using moored

ADCP velocity measurement were shown in section 4.



4. Results

<4-1 Properties of ISWs>

An example wave before and after the iterative algorithm are shown in Figs. 4-1 and 4-2, respectively. The current velocities U , V , W are shown at upper three panels. Wave properties, η , θ and C are shown in the left, middle, and right of bottom panel. The applied method removed the beam-spreading effect and restructured the velocity data of ISW with subtracting the modulated background flow. The Deming regression was applied to estimate C , to substitute for the standard linear regression when both fitted and reference variables ($\partial u'/\partial t$ and $\partial w/\partial z$) are subject to the intrinsic random noise of ADCP velocity measurements.

At LR1, eighteen events of ISW were converged through the algorithm and twenty events for LR4. The estimated wave properties for ISWs at LR1 and LR4 are summarized in Tabs. 4-1 and 4-2, respectively.

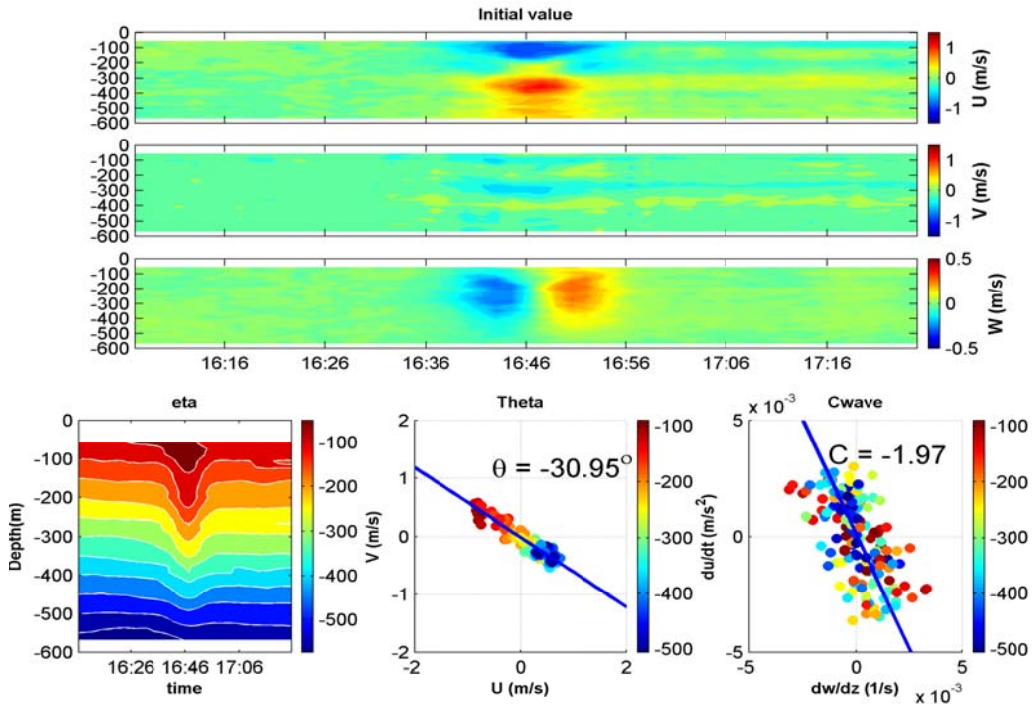


Fig. 4-1 Wave properties before iterative algorithm.

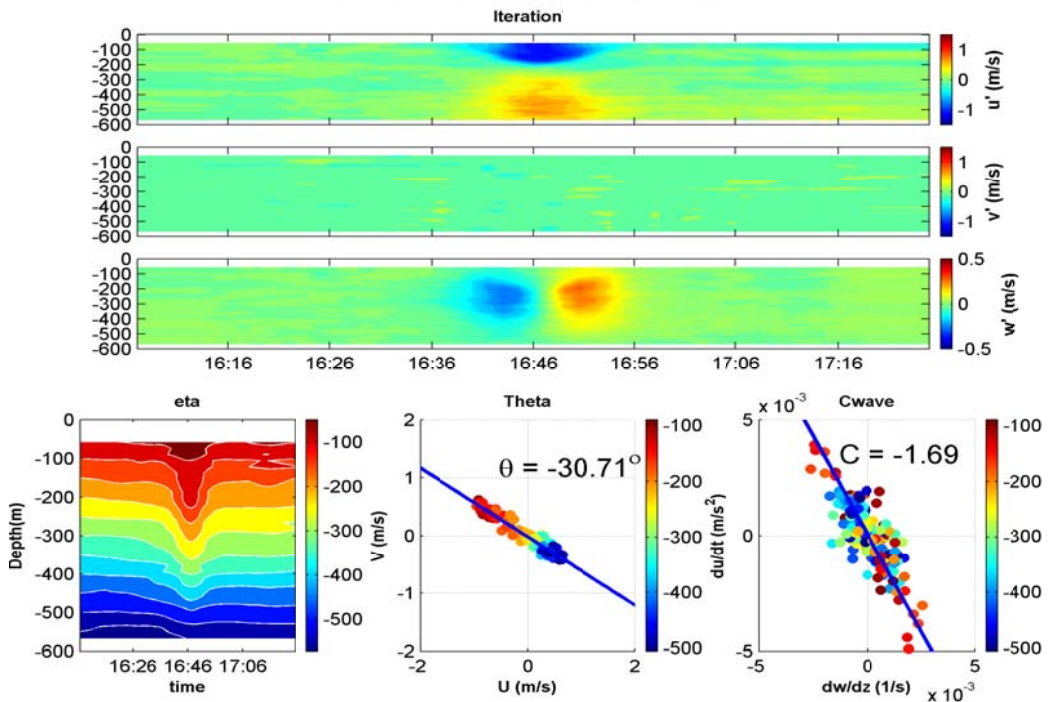


Fig. 4-2 Wave properties after iterative algorithm.

Tab. 4-1

ISWs at LR1

No.	Time	η (m)	θ	C (m/s)	$P_{measure}$ (dbar)	$P_{estimate}$ (dbar)	P_{nh} (dbar)
1	2007/4/17 05:23	-113.9	- 41.2°	-1.90	-0.20	-0.16	0.02
2	2007/4/17 16:46	-129.9	- 30.7°	-1.69	-0.16	-0.12	0.03
3	2007/4/18 05:40	-126.7	- 27.2°	-2.10	-0.28	-0.20	0.03
4	2007/4/18 16:58	-166.2	- 35.3°	-1.94	-0.25	-0.20	0.04
5	2007/4/19 05:44	-173.7	- 30.4°	-1.69	-0.26	-0.22	0.03
6	2007/4/19 17:58	-229.1	- 28.7°	-1.82	-0.32	-0.24	0.07
7	2007/4/20 19:37	-137.8	- 27.0°	-1.77	-0.28	-0.20	0.03
8	2007/4/22 23:05	-157.1	- 27.1°	-1.84	-0.24	-0.25	0.04
9	2007/4/23 07:22	-176.4	- 20.2°	-1.60	-0.24	-0.23	0.04
10	2007/4/24 09:26	-146.9	- 28.2°	-1.66	-0.10	-0.11	0.03
11	2007/4/25 11:20	-84.2	- 33.2°	-1.82	-0.08	-0.10	0.01
12	2007/4/30 06:13	-72.4	- 11.5°	-1.56	-0.09	-0.06	0.01
13	2007/5/02 05:38	-136.3	- 19.8°	-2.22	-0.25	-0.24	0.03
14	2007/5/02 19:10	-123.5	- 22.6°	-2.13	-0.15	-0.14	0.02
15	2007/5/03 05:22	-188.2	- 15.9°	-1.74	-0.32	-0.22	0.06
16	2007/5/04 05:37	-177.4	- 15.2°	-1.89	-0.30	-0.27	0.06
17	2007/5/05 05:55	-206.8	- 17.5°	-1.44	-0.26	-0.21	0.07
18	2007/5/06 05:59	-197.7	- 30.1°	-1.70	-0.25	-0.20	0.07
Average		-152.5	- 25.1°	-1.81	-0.22	-0.19	0.04

Tab. 4-2

ISWs at LR4

No.	Time	η (m)	θ	C (m/s)	$P_{measure}$ (dbar)	$P_{estimate}$ (dbar)	P_{nh} (dbar)
1	2007/4/16 10:22	-51.2	-66.3°	-1.41	-0.09	-0.08	0.01
2	2007/4/17 22:25	-164.6	-40.0°	-1.17	-0.24	-0.20	0.02
3	2007/4/23 13:51	-107.0	-07.6°	-0.69	-0.11	-0.09	0.02
4	2007/5/02 11:34	-45.5	-15.9°	-1.16	-0.11	-0.07	0.03
5	2007/5/03 11:27	-44.7	-24.3°	-1.23	-0.09	-0.09	0.03
6	2007/5/04 11:25	-66.5	-23.4°	-1.18	-0.18	-0.13	0.02
7	2007/5/05 12:12	-116.9	-30.9°	-0.95	-0.18	-0.16	0.03
8	2007/5/07 13:07	-112.4	-25.6°	-1.16	-0.16	-0.16	0.03
9	2007/5/08 14:27	-73.7	-29.5°	-1.04	-0.11	-0.09	0.03
10	2007/5/10 15:55	-84.8	-20.9°	-0.77	-0.09	-0.06	0.00
11	2007/5/15 22:04	-120.8	-36.6°	-1.31	-0.06	-0.07	0.02
12	2007/5/16 09:39	-65.3	-41.2°	-1.24	-0.12	-0.10	0.02
13	2007/5/17 10:03	-101.5	-18.9°	-0.93	-0.11	-0.12	0.01
14	2007/5/18 10:54	-145.4	-27.3°	-1.23	-0.23	-0.23	0.04
15	2007/5/20 01:28	-86.4	-53.2°	-1.32	-0.11	-0.10	0.02
16	2007/5/22 13:39	-79.1	-63.0°	-1.97	-0.07	-0.06	0.02
17	2007/6/01 09:03	-62.3	-08.5°	-1.73	-0.08	-0.08	0.02
18	2007/6/03 09:30	-79.1	-28.3°	-0.94	-0.09	-0.08	0.04
19	2007/6/05 10:49	-89.8	-07.0°	-0.80	-0.09	-0.06	0.03
20	2007/6/06 10:54	-92.8	-17.1°	-1.00	-0.12	-0.08	0.06
Average		-89.5	-29.3°	-1.16	-0.12	-0.11	0.03

< 4-2 Non-hydrostatic pressure >

The near full-depth ADCP velocity measurements permit the data to determine the vertical accelerations (Dw/Dt) that contribute to the near bottom non-hydrostatic pressure P_{nh} (Eq. (3.13)). Unfortunately, since we don't have the *in situ* time varying density profile and the velocity data at the surface, we can't estimate the other two decomposed seafloor pressure disturbance ($P_{h\eta}$ and P_{hp}).

With the assumption that wave propagates past the mooring site at an constant propagation speed C without change of wave form, Eq. (3.8), the time series may be written as

$$\frac{Dw}{Dt} = \frac{\partial w}{\partial t} - \frac{u'}{C} \frac{\partial w}{\partial t} + w \frac{\partial w}{\partial z}. \quad (4.1)$$

Each component of Dw/Dt for the example ISW is shown in Fig. 4-3. From top to the bottom panels, are the u' , w , $\partial w/\partial t$, $u'\partial w/\partial x$, $w\partial w/\partial z$ and Dw/Dt , respectively.

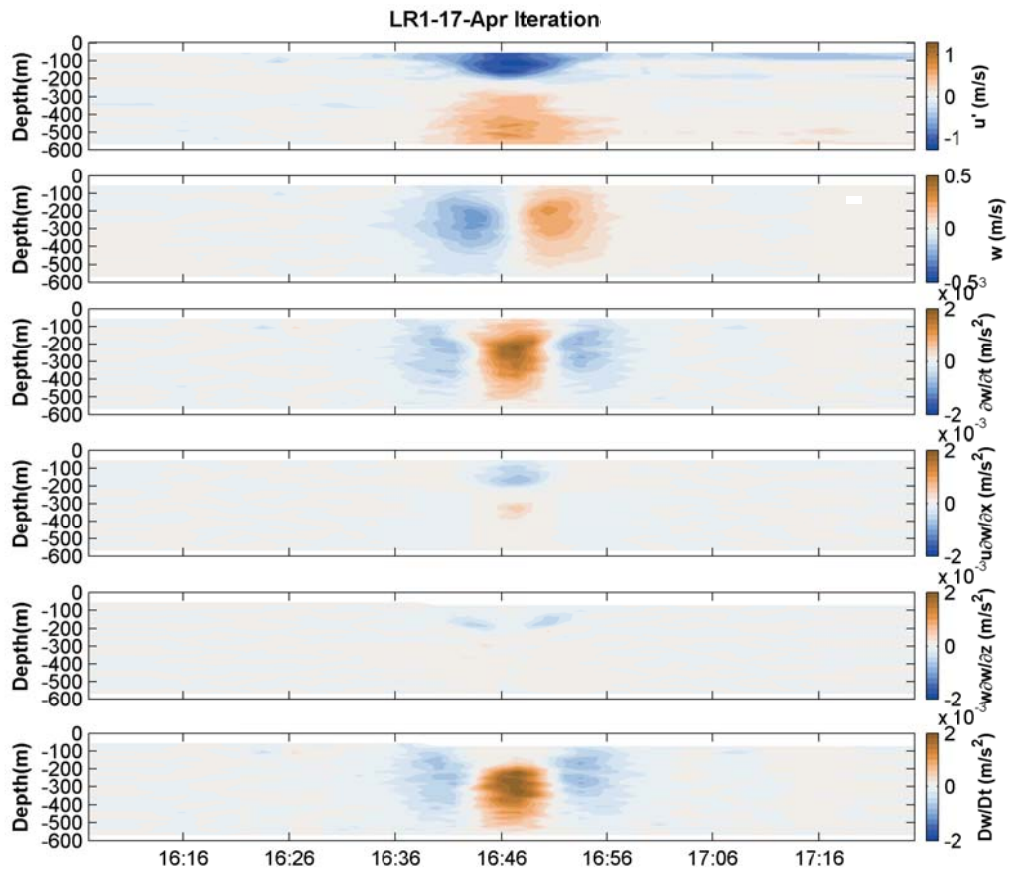


Fig. 4-3 The upper two panels shows the u' , w , of the example ISW shown in Fig. 2-6, with the correction of beam separate effect. The middle three panels shows the components of P_{nh} : $\partial w/\partial t$, $u'\partial w/\partial x$, $w\partial w/\partial z$, respective. Vertical acceleration, Dw/Dt , are shown at the last panel.

The estimated P_{nh} of this example ISW was shown in Fig. 4-4 (green line). It was estimated by a vertical integration of Dw/Dt via Eqs. (3.14) and (4.1)

$$P_{nh}|_{z_{p'}} = \rho_0 \int_{z_{p'}}^{H'} \frac{Dw}{Dt} dz = \rho_0 \int_{z_{p'}}^{H'} \frac{\partial w}{\partial t} - \frac{u'}{C} \frac{\partial w}{\partial t} + w \frac{\partial w}{\partial z} dz. \quad (4.2)$$

Because of the limitations of the ADCP measurements, the current velocity data are not available at the surface, we set the upper limit of integral as H' as the upper bound of the ADCP measurement rather than the water depth H . Also because of the first bin depth of the ADCP is actually about 30 m above bottom (upward-looking), we set the lower limit of integral as $Z_{p'}$ as the first bin depth of the ADCP rather than the seafloor where $z = 0$. The time-varying feature of the P_{nh} changes from negative ahead in front of the wave core to positive above the wave core to negative behind the wave core. The result was consistent with that concluded by Moum and Nash. (2008).

The peaks of estimated P_{nh} of ISWs at LR1 and LR4 are shown in Tabs. 4-1 and 4-2, respectively.

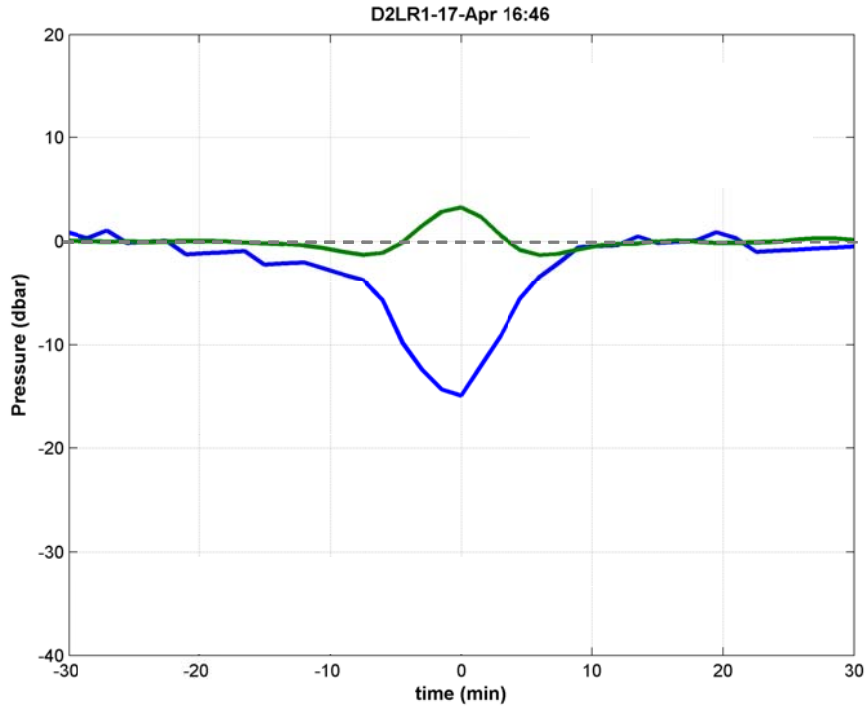


Fig. 4-4 The non-hydrostatic pressure disturbance (P_{nh} , green line) and the near bottom pressure disturbance estimated from Bernoulli function ($P_{Estimate}$, blue line) for the example ISW. The ISW signal was plotted in time coordinates with that peak time at $t=0$.

< 4-3 Total near bottom pressure >

The near bottom pressure disturbance due to the ISW ($P_{Estimate}$) was estimated from the Bernoulli function using the corrected velocity data and compared with the measured near bottom pressure data ($P_{Measure}$). The pressure gauge is located at 0.5 m above the bottom (z_p). However, because of the limitation of the instrument, the first bin depth of the ADCP velocity measurement is actually about 30 m above bottom (z_p'). For these mode-1 ISWs of depression, both density and vertical

velocity perturbations are comparatively weak near the bottom, we assume that both internal hydrostatic and non-hydrostatic pressures disturbance of mode-1 ISW is greatly attenuated toward the bottom. According to these, Eq. (3.18) become

$$P(z_p) \approx \frac{\rho}{2} \{C^2 - [u'(z_p) - C]^2\}. \quad (4.3)$$

Fig. 4-4 shows the estimate total near bottom pressure disturbance of the example ISW ($P_{Estimate}$, blue line). The amplitude of $P_{Estimate}$ of all ISW events at LR1 and LR4 are shown in Tabs. 4-1 and 4-2, respectively.

The comparisons of the wave form between $P_{Estimate}$ (blue line) and $P_{Measure}$ (black line) at LR1 and LR4 are present in Fig. 4-5. (Eighteen and twenty events were used at LR1 and LR4, respectively.) The $P_{Estimate}$ and $P_{Measure}$ were normalized by the amplitude of each wave. The ISW signal was plotted in time coordinates with that peak of $P_{Measure}$ occur at $t=0$. The occurrences of peaks of $P_{Estimate}$ were not exactly match with the occurrences of peaks of $P_{Measure}$, so that the average amplitude of normalized $P_{Estimate}$ was not one. The grey shaded areas indicate one standard deviation of $P_{Estimate}$ (Plus and minus). This result shows that the near bottom pressure disturbance could properly estimated from the calibrated moored ADCP velocity data.

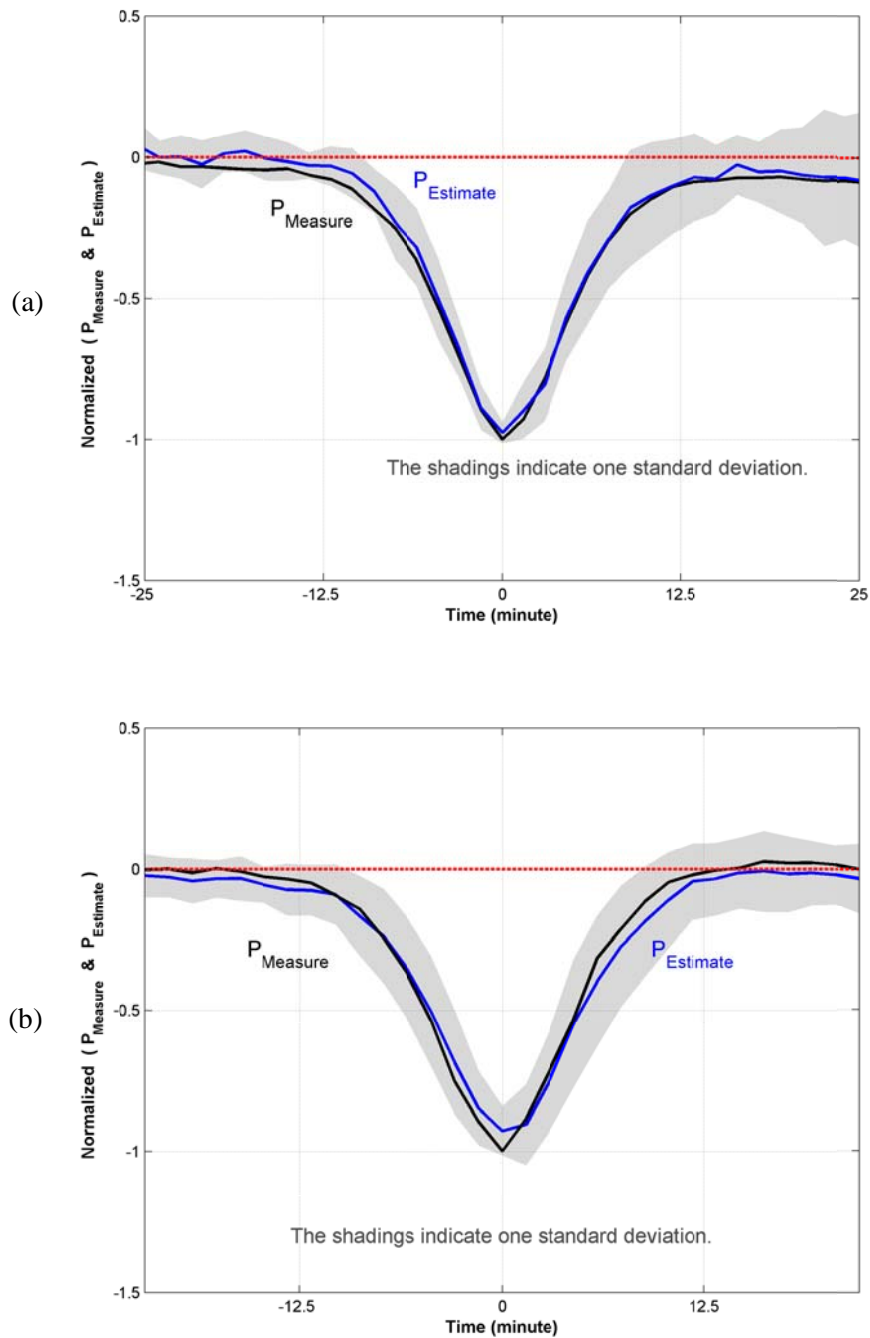


Fig. 4-5 The comparisons of the wave form between $P_{Estimate}$ (blue line) and $P_{Measure}$ (black line) at (a) LR1 and (b) LR4. The grey shaded areas indicate one standard deviation of $P_{Estimate}$. The ISW signal was plotted in time coordinates with that peak of $P_{Measure}$ occur at $t=0$.

Fig. 4-6 shows the comparison of the peaks of both $P_{Estimate}$ (blue dots) and P_{nh} (red dots) with $P_{Measure}$ at (a) LR1 and (b) LR4. The linear regression line and the coefficient of determination (R^2) are shown. As shown in the figure, the $P_{Measure}$ were consistently greater than $P_{Estimate}$. It is possible that, however, the current profile data did not include whole water column due to the limitation of ADCP measurement. As a consequence, the $P_{Estimate}$ would be underestimated. Fig. 4-4 also shows that the peaks of P_{nh} were linear proportional to the $P_{Measure}$.



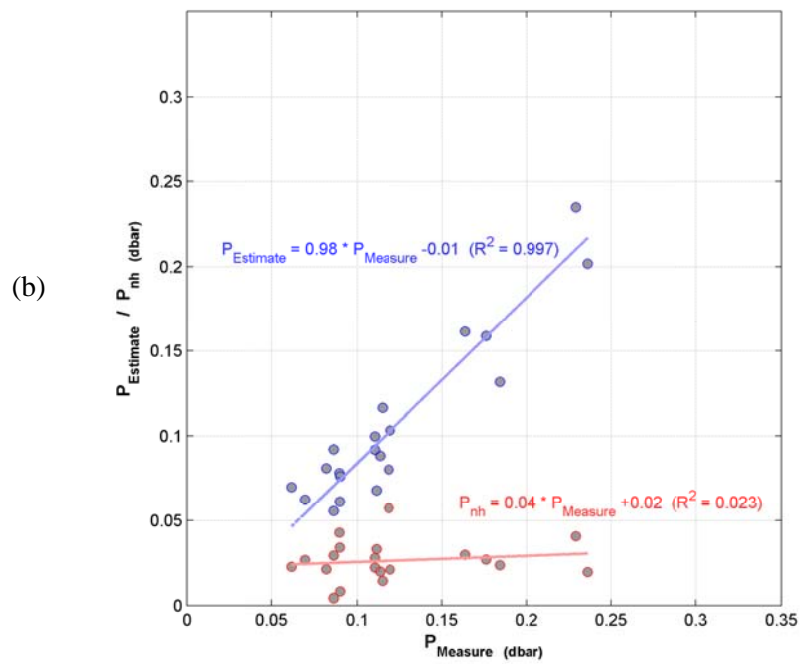
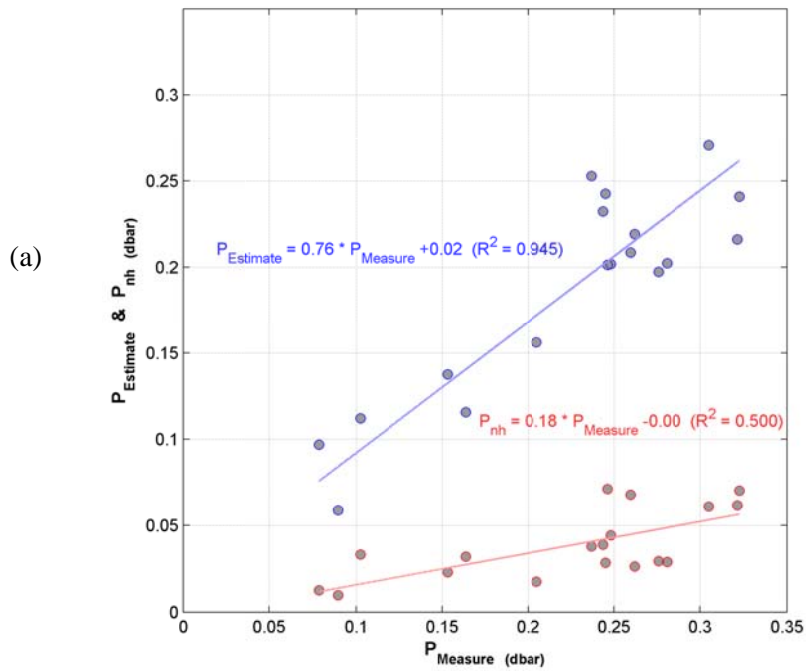


Fig. 4-6 Comparisons of the peaks between the $P_{Measure}$ and $P_{Estimate}$ (blue dots), and between the $P_{Measure}$ and P_{nh} (red dots) at (a) LR1 and (b) LR4, respectively. The linear regression line and the coefficient of determination (R^2) are shown.

5. Discussion and Summary

< 5.1 ISW pressure and vertical displacement >

Fig. 5-5 shows the comparison between amplitude of $P_{Measure}$ and η at LR1 (blue dots) and LR4 (red dots), respectively. The linear regression line and the coefficient of determination (R^2) are shown. This result points out that the amplitude of ISW vertical displacement could be estimated from the bottom pressure gauge. The result also shows that $P_{Measure}$ and η were generally larger at LR1 than at LR4, it might probably be associated with the local depth.

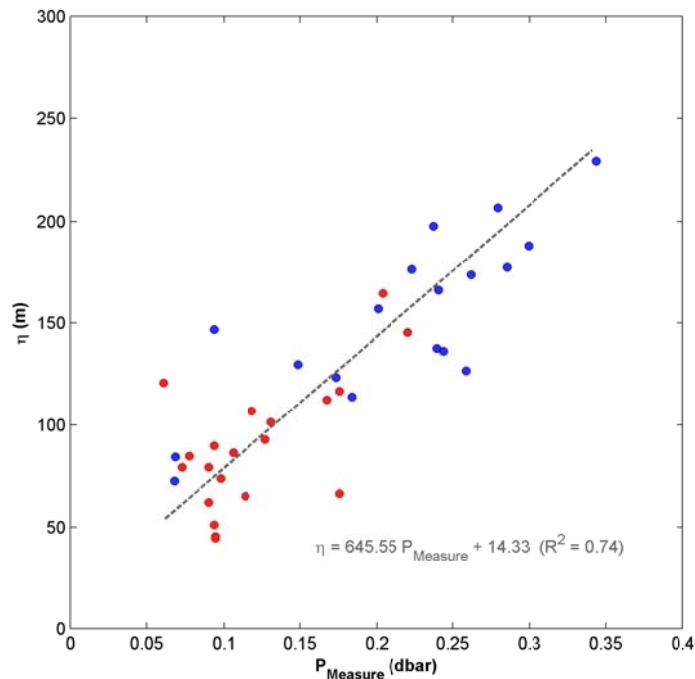


Fig.5-1 Comparison between amplitude of $P_{Measure}$ and η at LR1 (blue dots) and LR4 (red dots), respectively. The linear regression line and the coefficient of determination (R^2) are shown.

< 5.2 Summary >

The observed near bottom pressure fluctuation of tides were around 0.5-1.5 dbar, and that caused by ISWs were around 0.05-0.35 dbar. Using conventional methods, such as high-pass filter and harmonic analysis, to extract the pressure perturbation signal of ISW may degrades the ISW's near bottom pressure signal at the center of the wave and, even worse, it introduces biases by adding artificial pressure perturbations at the front and rear ends of the wave.

With the assumption that the two-dimensional ISW steady passing the mooring site with uniform propagation speed and without change of the wave form. The decomposed near bottom pressure perturbation due to ISWs could estimate from calibrated ADCP velocity data. For estimate the decomposed seafloor pressure disturbance associated with ISWs from the ADCP velocity measurements, we need to extract the wave signal and investigate the wave properties first. An iterative algorithm, developed by Chang *et al.* (2011), was applied to calibrated ADCP data and estimate the wave properties.

P_{nh} was estimated from the vertical momentum equation and $P_{Estimate}$ was estimated from the Bernoulli equation. The result of estimated P_{nh} indicated that the amplitude of P_{nh} is proportional to the $P_{Measure}$. The maximum of P_{nh} was 0.07 dbar

at LR1 on May 06, and the maximum of $P_{Estimate}$ was 0.27 dbar at LR1 on May 04.

The bias of ISW pressure estimated from uncorrected ADCP velocity data could reach to 0.35 dbar, which equivalent to the pressure disturbance caused by an ISW with η amplitude around 220 m

The comparison of the normalized $P_{Estimate}$ and $P_{Measure}$ shows that the prediction of the form of the ISW signal from Bernoulli equation is consist with the measured data. However, the comparison of the amplitude of $P_{Estimate}$ and $P_{Measure}$ shows that $P_{Measure}$ were consistently greater than $P_{Estimate}$. This is possibly from the leaking of full-water column velocity data. As a consequence, we have certainly underestimated the $P_{Estimate}$.

The amplitude of η and P_{nh} of mode-1 ISW was proportional to the total pressure, it point out that the amplitude of η and P_{nh} could estimated from the bottom pressure gauge in the continental slope of northern SCS.

Appendix

< a. Coordinate system of phase-lagged beam-to-earth transformation >

This section describes the coordinate systems of ISW and ADCP, and formulas of phase-lagged beam-to-earth transformation according to Chang *et al.* (2011). Fig. A-1 is the illustration of an ISW steady passing an ADCP mooring at a uniform propagation speed C . The ADCP has four beams (the along beam velocities are denote as $b_1, b_2, b_3,$ and b_4) of 20° transducer (ϕ) from vertical, and is fixed in earth coordinates so that b_1 and b_2 are aligned on the east-west direction, and b_3 and b_4 on the north-south direction. The vertical distance from the transducer head is d . The ISW propagation direction, which respect to the b_1 - b_2 axis, is now consistent with the propagation direction respect to the east-west axis (θ).

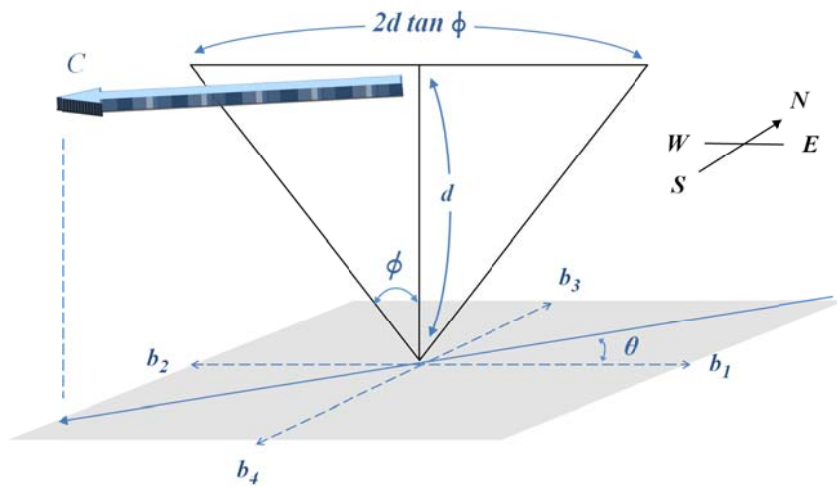


Fig. A-1 The illustration of an ISW steady passing an ADCP mooring.

Fig. A-2 shows the top view of Fig, A-1. The time required by wave front to move from one beam to the opposite are s_x and s_y

$$s_x = \frac{2d \tan \phi}{C/\cos(\theta)}, \quad (\text{A.1})$$

$$s_y = \frac{2d \tan \phi}{C/\sin(\theta)}. \quad (\text{A.2})$$

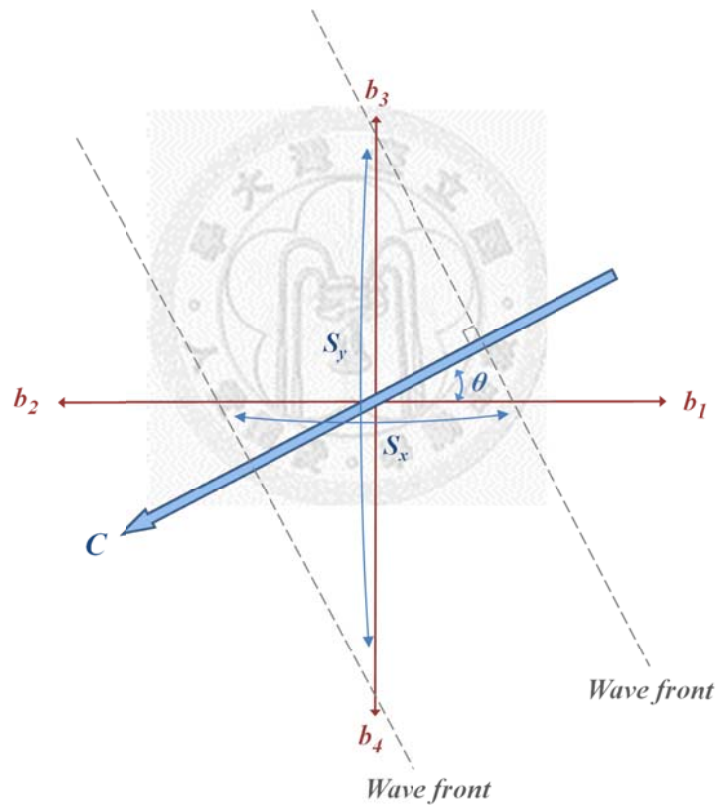


Fig. A-2 the top view of Fig, A-1.

Fig. A-3 shows the x - z plane view of Fig. A-1. The horizontal and vertical

components of b_1 are b_{1x} and b_{1z}

$$b_{1x} = \frac{b_1}{\sin \phi}, \quad (\text{A.3})$$

$$b_{1z} = \frac{b_1}{\cos \phi}. \quad (\text{A.4})$$

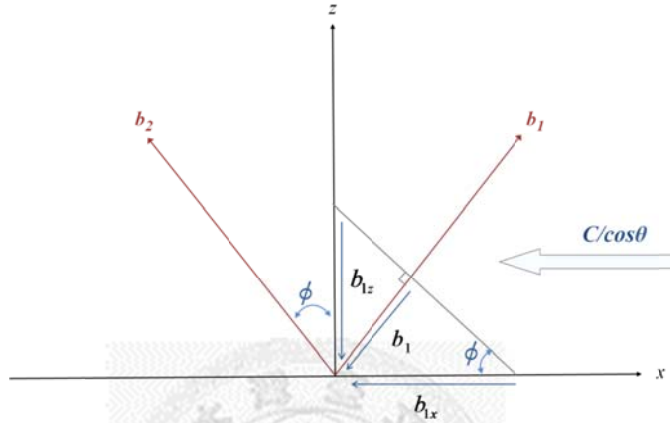


Fig. A-3 The x - z plane view of Fig. A-1.

Consequently, the mismatch in timing of the beam measurements could be corrected by introducing the lagged beam-to-earth transformation:

$$u = \frac{\frac{b_1(t - \frac{s_x}{2})}{\sin \phi} - \frac{b_2(t + \frac{s_x}{2})}{\sin \phi}}{2}, \quad (\text{A.5})$$

$$v = \frac{\frac{b_3(t - \frac{s_y}{2})}{\sin \phi} - \frac{b_4(t + \frac{s_y}{2})}{\sin \phi}}{2}, \quad (\text{A.6})$$

$$w = \frac{\frac{b_1(t - \frac{s_x}{2})}{\cos \phi} + \frac{b_2(t + \frac{s_x}{2})}{\cos \phi} + \frac{b_3(t - \frac{s_y}{2})}{\cos \phi} + \frac{b_4(t + \frac{s_y}{2})}{\cos \phi}}{4}, \quad (\text{A.7})$$

More generally, for an ISW steady passing an ADCP mooring with an arbitrary ADCP heading hd . The top view is shown in Fig. A-4. The ISW propagation direction (respect to the b_1 - b_2 axis) is not equivalent with the propagation direction respect to the east-west axis (θ). The ISW propagation direction is now : $\theta + hd$, and Eqs. A.1 and A.2 becomes:

$$s_x = \frac{2d \tan \phi \cos(\theta + hd)}{C}, \quad (\text{A.8})$$

$$s_y = \frac{2d \tan \phi \sin(\theta + hd)}{C}. \quad (\text{A.8})$$

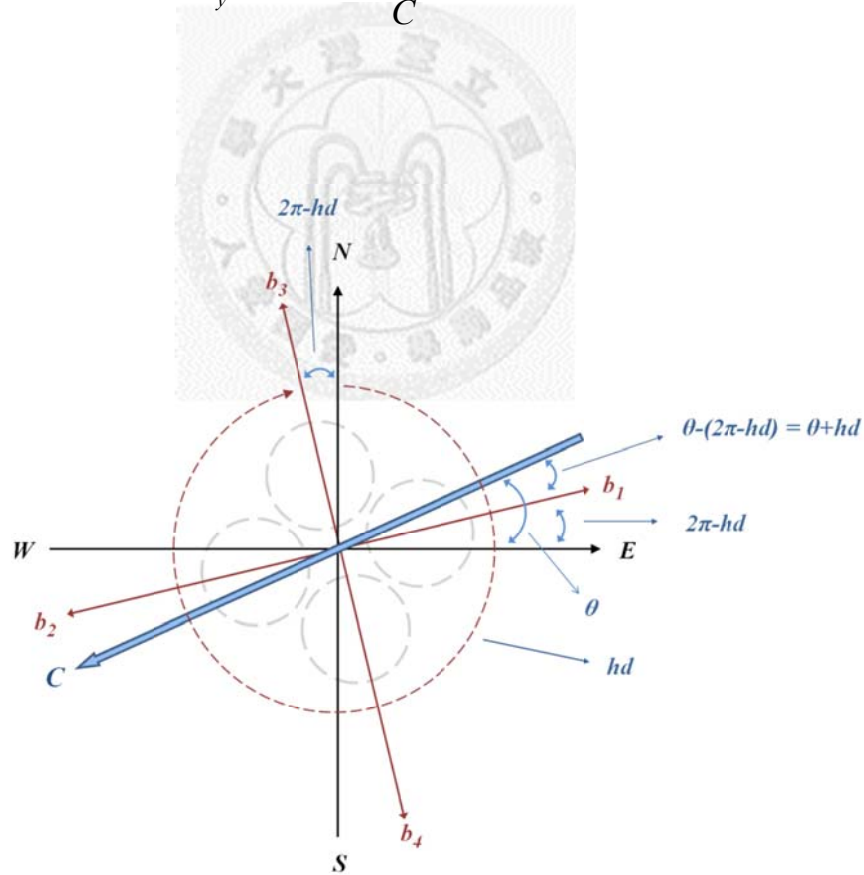


Fig. A-4 A wave steady passing the ADCP mooring with an arbitrary ADCP heading hd .

References

Apel, J. R., L. A. Ostrovsky, Y. A. Stepanyants, and J. F. Lynch, 2007: Internal solitons in the ocean and their effect on underwater sound. *J. Acoust. Soc. Amer.*, **121**, 695–722.

Alford M., R. -C. Lien, H. Simmons, J. Klymak, S. Ramp, Y. J. Yang, T. Y. Tang and M. -H. Chang, 2010: Speed and Evolution of Nonlinear Internal Waves Transiting the South China Sea, *J. Phys. Oceanogr.*, **40**, 1338-1355

Chang, M. -H., R. -C. Lien, T. Y. Tang, E. A. D'Asaro, and Y. J. Yang, 2006: Energy flux of nonlinear internal waves in northern South China Sea. *Geophys. Res. Lett.*, **33**, L03607.

Chang, M. -H., R. -C. Lien, Y. J. Yang, T. Y. Tang, 2011: Nonlinear Internal Wave Properties Estimated with Moored ADCP Measurements. *J. Atmos. Oceanic Technol.*, **28**, 802–815.

Farmer, D. and L. Armi, 1999: The generation and trapping of solitary waves over

topography. *Science*, **283**, 188-190.

Haury, L.R., M.G. Briscoe and M.H. Orr, 1979: Tidally generated internal wave packets in Massachusetts Bay. *Nature*, **278 (5702)**, 312-317.

Hsu, M. K., A. K. Liu, and C. Liu, 2000: A study of internal waves in the China Seas and Yellow Sea using SAR. *Continental Shelf Research*, **20**, 389–410.

Liu, A. K., J. R. Apel, and J. R. Holbrook, 1985: Nonlinear internal wave evolution in the Sulu Sea. *J. Phys. Oceanogr.*, **15**, 1613-1624.

Lien, R.-C., T. Y. Tang, M. H. Chang, and E. A. D'Asaro, 2005: Energy of nonlinear internal waves in the South China Sea. *Geophys. Res. Lett.*, **32**, L05615.

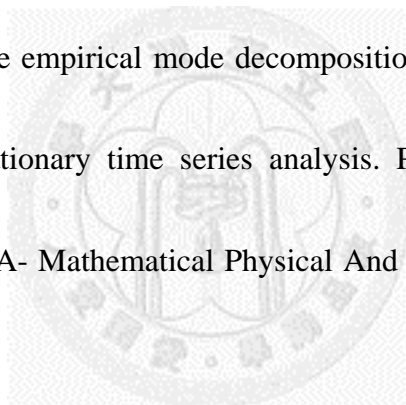
Moum, J. N., Gregg, M. C., Lien, R. C. & Carr, M, 1995: Comparison of turbulence kinetic energy dissipation rate estimates from two ocean microstructure profilers. *J. Atmos. Ocean. Technol.*, **12**, 346 – 366.

Moum, J. N., and W. D. Smyth, 2006: The pressure disturbance of a nonlinear internal wave train. *J. Fluid Mech.*, **558**, 153–177.

Moum, J. N., J. D. Nash, 2008: Seafloor Pressure Measurements of Nonlinear Internal Waves. *J. Phys. Oceanogr.*, **38**, 481–491.

N.E. Huang, Z. Shen, S.R. Long, M.L.C. Wu, H.H. Shih, Q.N. Zheng, N.C. Yen, C.C.

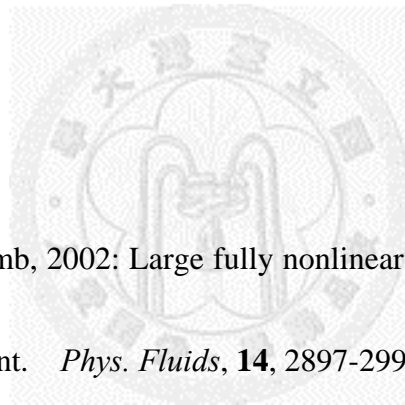
Tung, H.H. Liu, 1998: The empirical mode decomposition and the Hilbert spectrum for nonlinear and non-stationary time series analysis. Proceedings Of The Royal Society of London Series A- Mathematical Physical And Engineering Sciences, **454**, 903-995



Qiang Li, David M. Farmer, Timothy F. Duda, and Steve Ramp, 2009: Acoustical Measurement of Nonlinear Internal Waves using the Inverted Echo Sounder, *J. Atmos. Oceanic Technol.*, **26**, 2228-2242.

Rich Pawlowicz, Bob Beardsley, and Steve Lentz, 2002: Classical tidal harmonic analysis including error estimates in MATLAB using T_TIDE. *Computers and Geosciences*, **28**, 929-937.

Ramp, R. S., T. Y. Tang, T. F. Duda, J. F. Lynch, A. K. Liu, C.-S. Chiu, F. Bahr, H.-R. Kim, and Y. J. Yang, 2004: Internal solitons in the northeastern South China Sea Part I: Source and deep water propagation. *IEEE J. Oceanic Eng.*, **29**, 1157-1181.



Stastna, M., and K. G. Lamb, 2002: Large fully nonlinear internal solitary waves: the effect of background current. *Phys. Fluids*, **14**, 2897-2999.

Scotti, A., B. Butman, R. C. Beardsley, P. S. Alexander, and S. Anderson, 2005: A modified beam-to-earth transformation to measure short-wavelength internal waves with an acoustic Doppler current profiler. *J. Atmos. Oceanic Technol.*, **22**, 583–591.

Yang, Y. J., T. Y. Tang, M. H. Chang, A. K. Liu, M.-K. Hsu, and S. R. Ramp, 2004,
Solitons northeast of Tung-Sha Island during the ASIAEX pilot studies, *IEEE J.
Oceanic Eng.*, **29**, 1182– 1199.

Zhao, Z., V. Klemas, Q. Zheng, and X.-H. Yan, 2004: Remote sensing evidence for
baroclinic tide origin of internal solitary waves in the northeastern South China Sea.
Geophys. Res. Lett., **31**, L06302.

